LASER & PHOTONICS REVIEWS
www.lpr-journal.org

In-Source High-Resolution Spectroscopy Using an Integrated Tunable Raman Laser

Eduardo Granados, Georgios Stoikos, Cyril Bernerd, Katerina Chrysalidis, Daniel T. Echarri, Valentin N. Fedosseev, Reinhard Heinke, and Bruce A. Marsh*

Dedicated to the memory of Steve Edstrom

Tunable single-frequency lasers are the most prominent tool for high-resolution spectroscopy, allowing for the study and exploitation of the electronic structure of atoms. A significant milestone relies on the demonstration of integrated laser technology for performing such a task. The device presented here is composed of a compact Fabry–Perot monolithic resonator capable of producing tunable and Fourier-limited nanosecond pulses with a MHz-class frequency stability without active cavity stabilization elements. It also has the remarkable capability of exploiting the Raman effect to funnel efficiently the broad spectrum of an input laser to a spectrally-bright Stokes pulse at hard-to-access wavelength ranges. The targeted atom for the demonstrations is ^{152}Sm, released as an atomic vapor in a hot cavity environment. Here, the Stokes field is tuned to a wavelength of 433.9 nm, while a crossed-beams spectroscopy setup is used to minimize the Doppler broadened spectral features of the atoms. With this work, the suitability of integrated diamond Raman lasers as a high-resolution in-source spectroscopy tool is demonstrated, enabling many applications in atomic and nuclear physics. The integrated form-factor and inherent simplicity makes such a laser an interesting prospect for quantum-technology based sensing systems and related applications.

1. Introduction

Deep knowledge of the forces and interactions inside nuclei is the basis for understanding and controlling atomic processes in a wide range of application areas, including atomic clocks,[1,2] quantum computing,[3,4] or nuclear spectroscopy.[5] A gateway to access this information is through the interplay between the electronic and nuclear structure of atoms that is, hyperfine interactions. These interactions are minuscule compared to the dominating thermal and electromagnetic effects occurring in atoms, fueling the need for high precision and Doppler-free techniques of spectroscopic measurement. Hyperfine spectroscopy reveals highly valuable information related to nuclear properties and atomic structures, including nuclear shape, size and the individual multipole structure of isotopes and isomers all across the chart of nuclides.[6]

The hyperfine states of trapped ions are commonly used for storing qubits in ion-trap quantum computing, thanks to their extended excited state lifetimes.[7] Pairs of laser pulses are used here to drive the transition by having their frequency difference equal to the specific transition's frequency. In general, kHz to MHz linewidth lasers are the necessary tool to cool, selectively excite and ionize atomic species.[2] Integrating such laser sources on a chip is poised to provide the scalability necessary for quantum technology-based sensing systems and applications,[8] but advances are still required in miniature lasers with output in the ultraviolet (UV) and visible spectral range as well as low-loss passive devices such as couplers and waveguides.[4,9] Notably, a substantial portion of the spectrum ranging from the UV to the near-infrared (IR) is only recently becoming accessible using state-of-the-art integrated photonic devices.[10,11]

The production itself of pure ion beams also profits from efficient and tunable narrow linewidth laser sources. Here, Resonance Ionization Spectroscopy is a common technique that enables element-selective ionization by using a series of tunable laser sources matched to the appropriate transitions of an ionization scheme. The selectivity is achieved by consecutive resonant electron excitations, eventually leading above the ionization potential. Once the ions are produced, they can be trapped and manipulated by employing electromagnetic fields. The laser sources used here, besides being energy-matched to the transition (normally in the UV-visible spectral range), are also matched in linewidth to the experimental conditions of the laser-atom interaction for maximum ionization efficiency and must be continuously tunable across the transition for spectroscopy

E. Granados, G. Stoikos, C. Bernerd, K. Chrysalidis, D. T. Echarri, V. N. Fedosseev, R. Heinke, B. A. Marsh
CERN
Geneva 1217, Switzerland
E-mail: eduardo.granados@cern.ch

The ORCID identification number(s) for the author(s) of this article can be found under https://doi.org/10.1002/lpor.202300564

DOI: 10.1002/lpor.202300564

applications. The resulting ion rate is determined by the degree of saturation of the resonant transitions, the statistical weights of the electronic energy levels involved, the laser-atom interaction duty cycle and the ion survival and extraction efficiency.[12] If a particular measurement or application requires the resolution of the hyperfine structure of an atomic level, a compromise between ionization efficiency and spectral resolution can be made and narrow-linewidth (MHz-range) tunable lasers are used, with below-saturation laser power. In such applications laser power and wavelength stability become crucial parameters.

In this paper, we demonstrate the suitability of an integrated tunable single-frequency Raman laser operating in the 430 nm spectral region for the aforementioned high-resolution spectroscopy applications. The experiments were carried out in a Doppler-reduced geometry utilizing crossed laser beams interacting with samarium atoms effusing from a hot-cavity capillary under high-vacuum (10^{-6} mbar) conditions.[13] We target a narrow linewidth transition of ^{152}Sm -with no hyperfine splittings- in order to unequivocally measure the cumulative resolution and sensitivity of our spectroscopic setup. The results are accompanied by end-to-end Monte Carlo particle tracing simulations of the thermal and effusion effects at the ion source, which greatly influence the overall achievable spectral resolution, as well as a Raman laser model for predicting the spectral purity achievable using a monolithic Raman laser platform.

2. Integrated Tunable Diamond Raman Lasers

There is keen interest in the photonic integration of widely tunable, high-performance MHz-and kHz-class narrow-band lasers at a wavelength, typically in the UV-visible spectral range, to excite atomic transitions in a Doppler-reduced geometry.[14–16] Traditionally, free-space lasers including injection-seeded dye and Ti:Sapphire lasers have been used for this purpose,[17] However, these require a complex, expensive and bulky suite of systems to produce and stabilize the required narrow-band pulsed laser light, and they are not integrable on a chip. Recent efforts have been made to simplify this but it remains a significant technical challenge.[18]

Stimulated Raman scattering (SRS) offers an alternative approach. Unlike traditional ion-based lasers, the emissions from Raman lasers are not limited to the specific emission cross-section of ions since it uses virtual levels based on the interaction of light with phonons. This provides unique advantages such as access to unconventional wavelengths in the UV-visible range[19] and the mid-IR[20] and compatibility with laser sources operating within the transparency range of the SRS media. Additionally, SRS gain is not subject to spatial hole burning, simplifying the laser architecture to produce high quality single longitudinal mode light, and when using diamond as SRS media power scalability at high stability is achievable.[21–25] Furthermore, diamond resonators can be effectively integrated on a chip exhibiting very high quality factors.[26,27]

In terms of linewidth, the Stokes spectrum can resemble that of the pump in the so-called high Raman gain regime.[28,29] The Raman process can be further cascaded using multiple Stokes orders, extending the available spectral coverage at virtually no cost.[30,31] Embedding the laser resonator within the Raman media proved to have additional advantages, such as the ability to produce a frequency stable output directly from a monolithic Fabry–Perot resonator, circumventing the need of external mechanical feedback loops to control the cavity length. These miniaturized resonators can perform complex tasks, such as spectral funneling when pumped by GHz linewidth lasers (enhancing the available power spectral density (PSD) by 50×[32]), or achieve higher spectral brightness exploiting double resonances within the resonator.[33] Their spectral purity, particularly the residual intensity noise product of the Raman interaction, needs to be further studied in detail if these lasers are to be applied in high resolution spectroscopy setups.

Beyond generating narrow linewidth light at visible wavelengths, tuning integrated resonators in GHz frequency scales with high accuracy and repeatability is challenging. Acousto- and electro-optic modulators can provide shifts up to a few GHz but they normally operate in the infrared and produce parasitic sidebands.[34] Nonlinear $\chi^{(2)}$ and $\chi^{(3)}$ mixing processes can achieve efficient and tunable frequency conversion but requires strict phase-matching between the interacting waves, precise angular control of the optical components, and have a strong nonlinear dependence on optical power. Here, diamond Raman lasers provide the advantage of being accurately tuned by using temperature exclusively thanks to the outstanding thermal and thermo-optic properties of the material, in combination with the temperature dependence of the Raman shift.[35,36]

The optical setup used in this work comprises an integrated Fabry–Perot diamond resonator, similar to the one presented in [35]. The advantage of using such a diamond resonator in our spectroscopy experiments is threefold: First, the output Stokes pulse can be precisely tuned and its linewidth approaches the Fourier limit,[32] so it can be used in high-resolution spectral scans. Second, accessing a spectral range not to reduce the linewidth of the tunable pump laser to the Fourier limit so it can be used in high-resolution spectral scans. Second, accessing a spectral range not usually covered by standard laser gain media. Third, stabilizing and tuning its wavelength in a simple and reliable manner with MHz accuracy. While the precise tunability was achieved using the bulk diamond temperature, the coarse tunability was provided by the pump laser. **Figure 1**a shows the main experimental parameters used in this work, indicating a 10× enhancement in the power spectral density from pump to Stokes pulses taking into account a 40% power conversion efficiency and a linewidth reduction factor of 25× approximately.

2.1. Spectral Purity

Typical tunable nanosecond pump lasers feature noisy temporal structure due to their multi-mode spectral content. Here, the resulting pulse has features on timescales faster than the few-millimeter long diamond resonator round-trip time, and is caused by the interference of its multiple spectral modes. An example of such pulse is included in Figure 1b. Nevertheless, the amplitude and phase of the individual axial modes generally vary on the timescale of the round-trip time or slower. Since these timescales are generally longer than the Raman dephasing time, in most cases we can model the Raman process for each spectral mode using steady-state Raman theory, even if the interference of the pump axial modes produces a time structure that

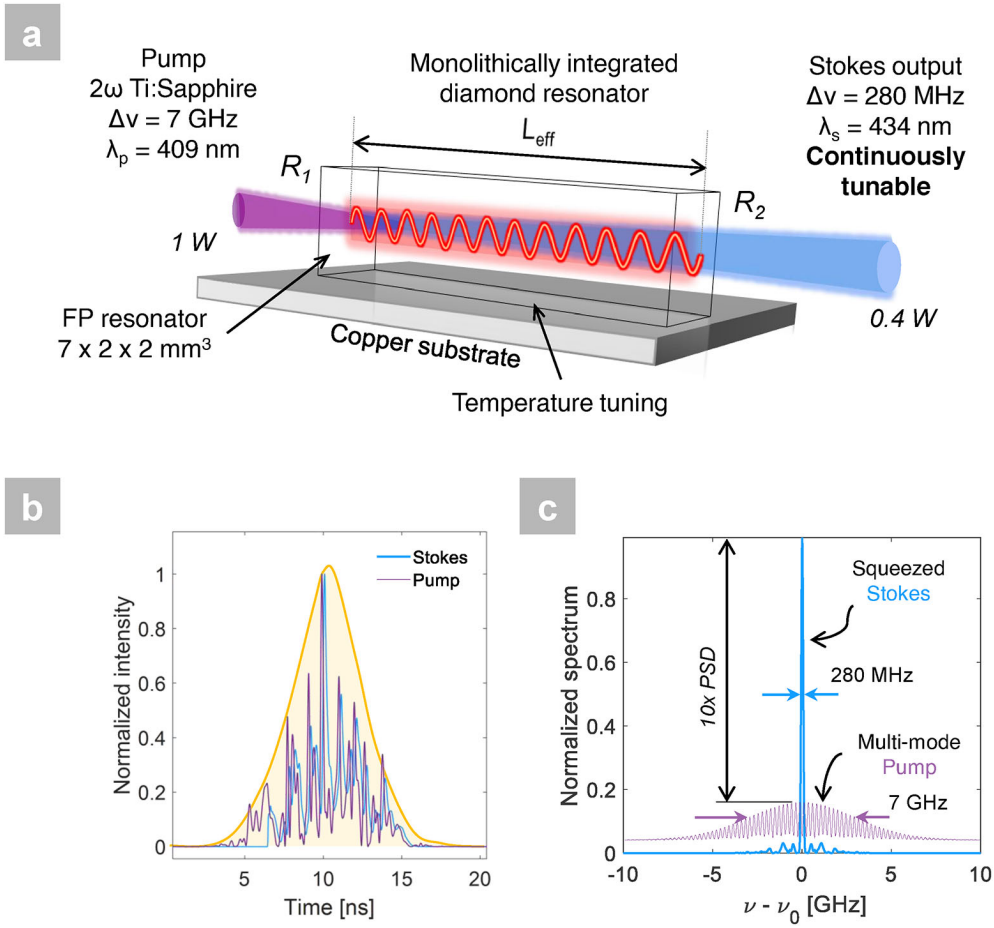

Figure 1. a) Monolithic diamond Raman resonator implementation of a tunable spectral squeezer: here the Fabry–Perot resonator formed by surfaces with reflectivities R_1 and R_2 and effective length L_{eff} is tuned using temperature exclusively. (b) and (c) show simulations of the spectral synthesis of a multi-mode Ti:Sapphire laser at 409.3 nm (second harmonic) with a linewidth of 7 GHz to a single axial mode Stokes pulse at 433.9 nm pulse, resulting in a linewidth reduction down to 280 MHz. The power spectral density (PSD) is enhanced by a approximately an order of magnitude (thanks to the 40% power conversion efficiency of the devices) while the temporal profile of the Stokes remains similar to that of the pump.

would need transient Raman theory if modeled in the time domain. This computationally-efficient approach has been widely used in the past to analyze SRS with multi-mode lasers,[37–43] and more recently to model phonon-resonant Raman interactions featuring efficient spectral squeezing in integrated diamond resonators.[32]

The interaction of pump and Stokes mode fields can be calculated using non-degenerate mode interactions. The pump modes are modeled as an ensemble of longitudinal modes, modulated by a Gaussian envelope representing the average pump laser linewidth. The Stokes modes, not to be confused with the axial modes within the Raman resonator, are seeded from noise and have the same mode spacing as the pump fields. We start then by writing the multi-mode fundamental with $2m+1$ modes spaced in frequency by Ω_F, and a multi-mode Stokes field with $2m+1$ modes spaced in frequency by Ω_F: $\tilde{E}_F = \sum_{l=-m}^{m} F_l e^{i(\omega_{F(l)}t - k_{F(l)}z)} + cc$ and $\tilde{E}_S = \sum_{l=-m}^{m} S_l e^{i(\omega_{S(l)}t - k_{S(l)}z)} + cc$ in which cc represents the complex conjugate of the preceding term, $\omega_{S(l)} = \omega_{S(0)} + \Omega_F l$, and $\omega_{F(l)} = \omega_{F(0)} + \Omega_F l$. In these equations, S_l and F_l are complex amplitudes describing the amplitude and phase of the modes travelling inside the diamond.

The Raman simulation includes all the possible mode interactions between these pump and Stokes modes. The result is then modulated by the diamond resonator spectral response, producing the longitudinal modes of the resonator. We calculate the residual intensity noise (RIN) of the Stokes field in the spectral domain. This quantity is particularly important in spectroscopy applications, where the signal-to-noise ratio achievable in a spectral scan enables the identification of transitions with distinct absorption cross sections.

In order to describe the coupling between the pump and Stokes set of modes, we rely on steady-state Raman formalism and write it in a non-degenerate mode for four generic modes, two pump field modes F_{l_1}, F_{l_2} with two Stokes field modes S_{l_3} and S_{l_4} as:

$$\frac{1}{u_S}\frac{\partial S_{l_4}}{\partial t} \pm \frac{\partial S_{l_4}}{\partial z} \propto F_{l_1}(F^*_{l_2} S_{l_3}) \tag{1}$$

in which u_S is the group velocity at the Stokes wavelength. This mixing can be interpreted as two pump modes $(F^*_{l_2} S_{l_3})$ driving a

phonon field and a third mode F_{l_1} scattering off the phonon field to drive a fourth mode S_{l_4}.[37] For fundamental and Stokes pulsed fields with many longitudinal modes or broadband modes, in principle all types of interactions can drive a polarization at the frequency of a generic mode S_{r_2}, given that they satisfy the equation $\omega_{S_{r_2}} = \omega_{F_{l_1}} - \omega_{F_{l_2}} + \omega_{S_{r_1}}$. The interaction thus produces the mentioned spectral side-modes affecting the reliability of the laser for high sensitivity spectroscopy applications. The full description of the computational model can be found in the supplemental materials alongside with theoretical results.

The result in the time domain shows a Stokes pulse quickly following the shape of the pump pulse, due to the low reflectivity of the resonator (Figure 1b). As the reflectivity of the resonator is increased, the output Stokes pulse becomes smoother due to the low-pass filtering effect of the resonator. In this regime the resonator is acting similarly to photonic flywheels and optical integrators.[44] Figure 1c shows the spectrum result using this model for the experimental parameters, in which the spectral structure of the Stokes field can be easily observed. The spectrum of the pump is squeezed from 7 GHz down to 280 MHz, at 40% conversion efficiency, yielding an enhancement in power spectral density of ten times. We computed the same simulation for different resonator quality factors by changing its reflectivity $R = R_1, R_2$. We found that this is indeed a simple way of enhancing its spectral purity. For example, the side-mode contribution at 2 GHz from the center Stokes frequency can be reduced from 25 dB to >50 dB by simply increasing R from 18% to 95% as depicted in **Figure 2**a, b. It should be noted, however, that an increase in the resonator quality factor can favor cascading into higher Stokes orders. The cascading effect can be minimized by implementing coatings with tailored spectral characteristics (high transmission at the higher order Stokes wavelengths for example).

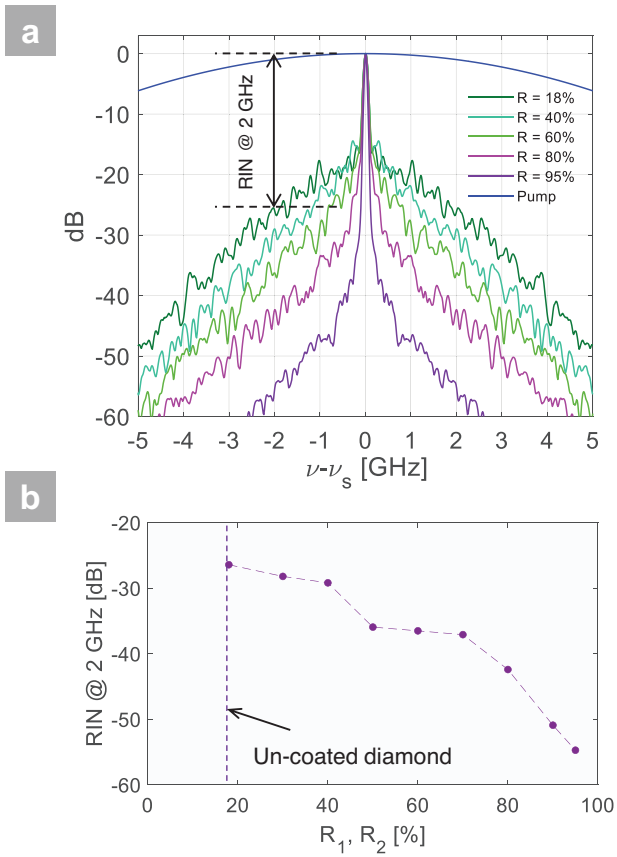

Figure 2. a) Model results of averaged Stokes spectra over 100 pulses for various values of R $=R_1, R_2$. b) Resulting relative intensity noise (RIN) at 2 GHz from the Stokes center frequency for several resonator reflectivities.

2.2. Experimental Performance

The Raman media was a synthetic, cuboid diamond crystal with dimensions of $7 \times 2 \times 2$ mm^3, plane-cut for beam propagation parallel to the ⟨100⟩ axis, free spectral range free-spectral-range (FSR) ≈ 8 GHz at 433.9 nm. The edges of the resonator, polished with parallelism better than 0.5 μ m mm^{-1}, were left un-coated. The Fresnel reflectivity ($R_{1,2} = 18\%$) was enough to guarantee efficient Raman operation. The temperature tuning of the resonator was conducted by placing the crystal on a copper substrate inside a high precision temperature controller (Covesion Ltd), with a stability better than 10 mK.

The diamond crystal was then pumped by a tunable, gain-switched frequency-doubled Ti:Sapphire laser operating at 409.3 nm with a maximum power of 1 W and a repetition rate of 10 kHz as shown in Figure 1b, producing a multi-mode 7 GHz wide spectrum. The pump was focused by a bi-convex lens (f = 150 mm) to the center of the diamond crystal. Right after the resonator, a curved mirror (radius of curvature = 50 mm) was used to reflect and re-focus the pump beam, to improve overall conversion efficiency by providing the second pass within the diamond. After the Raman conversion, a dichroic mirror was used to separate the Stokes from the pump fields. The maximum average power of the Stokes radiation was 400 mW (40% conversion efficiency), with its power stability directly dependant on that of the pump.

The output Stokes wavelength tuning as a function of temperature was measured using a set of high resolution Fizeau interferometers (Atos wavemeter LM007). In **Figure 3**a the raw signal output of the highest resolution Fizeau interferometer (with FSR of 3.75 GHz and instrumental width of 449 MHz) is depicted, showing a continuous and linear tuning of the Stokes pulse in the entire temperature range.

Following the theory described in [35], the expected values for the tuning slope ($\Delta\nu_s/\Delta T$) in the range from 60–70 °C is approximately -3.2 GHz/°C, which agrees well with the experimentally measured values shown in Figure 3b. For this estimation, the thermo-optic coefficient was calculated using the model described in ref. [36], whereas the dispersion was calculated using the 2-factor Sellmeier equation for synthetic diamond found in ref. [45] and the thermal expansion coefficient of $\alpha \sim 1.1 \times 10^{-6}$ K^{-1} found in ref. [46]. Given that the measured stability for the resonator temperature was better than 10 mK, we estimate that the frequency accuracy of our Raman laser is better than 30 MHz. In our subsequent spectroscopy experiments, the resonator was placed outside the ion trap and therefore its temperature was not affected by the hot environment existing in the vicinity of the ion source. It can be observed in Figure 3b that the Stokes wavelength follows an irregular trend compared to

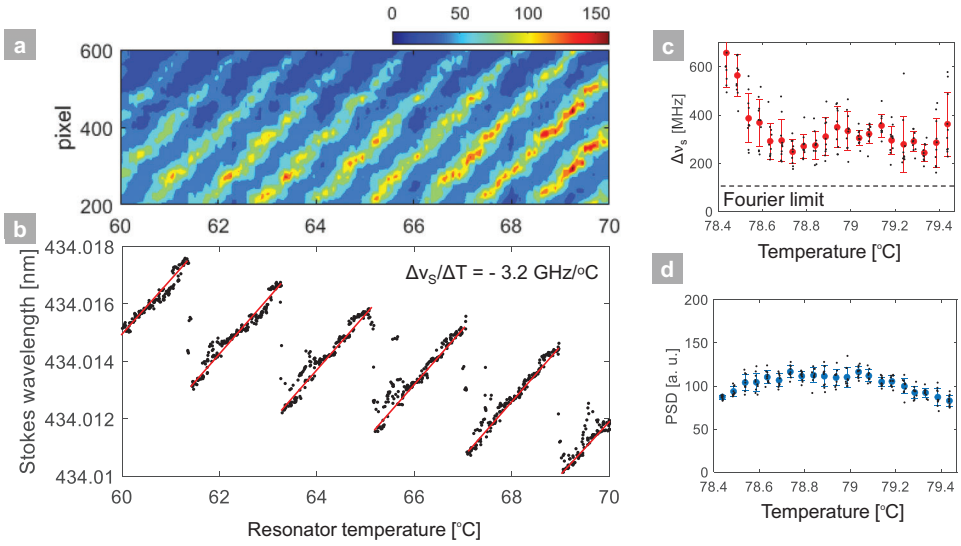

Figure 3. a) Fizeau interferometer pattern (colorbar proportional to CCD intensity) for different resonator temperatures. b) Stokes center wavelength as a function of measured diamond temperature. Red lines are linear fits to the tuning slope. c) Stokes linewidth $\Delta\nu_s$ as a function of temperature covering one FSR, compared to the Stokes pulse Fourier-limit. d) Power Spectral Density (PSD) stability for the same temperature range.

previous studies,[35,36] where the wavelength distribution along a single FSR is closer to a linear fit. The main effect leading to this behavior is related to the thermal equilibrium time of the bulk diamond. During the experiments, the rapid temperature setting -faster than the thermal equilibrium time of the resonator (of the order of 10 to 20 s)- resulted in a divergence between the measured temperature and the real bulk temperature, leading to deviations from the expected near-linear trend in Figure 3b.

The output average Stokes linewidth was $\Delta\nu_s \approx 300$ MHz and close to the Fourier-limit as is shown in Figure 3c in good agreement with theory. The linewidth became larger and up to 600 MHz at the edges of the FSR, owing to a decreased available gain as the Stokes is tuned further away from the spectral peak of the Raman gain. As it can be seen in Figure 3d the power spectral density (PSD), calculated using the measured spectrum and the Stokes pulse energy simultaneously, was relatively stable across the entire FSR of the diamond Raman resonator.

The Stokes laser was then guided to the experimental setup for perpendicular illumination of the atom beam, as the first-step transition of the two-step ionization process chosen for our demonstrations. The second step, in a collinear geometry, was performed using a non-resonant ionizing transition with a high power frequency-tripled Q-switched Nd:YAG laser, producing a maximum power of 10 W at 355 nm. Both lasers operate at 10 kHz and are synchronised by individual electronic Q-switch timing control of the initial pump sources.

3. Doppler-Reduced In-Source Spectroscopy Setup

The crossed-beam geometry used for this study was made possible through the use of the PI-LIST (Perpendicularly Illuminated Laser Ion Source and Trap),[47] based on the high-purity laser ion source LIST[48,49] of the radioactive ion beam facility ISOLDE at CERN[50] and is depicted in **Figure 4**a. This device takes advantage of the collimation of the atoms emerging from a tubular hot cavity geometry. The particle vector momentum is predominantly parallel to the axis z and collinear with respect to the ion beam. When a laser beam guided in a perpendicular direction to this axis z, it will see only the transverse component of the momentum spread of the atom beam, thus minimizing the Doppler effect. Furthermore, the subsequent ionization laser interacts only on the portion of the excited atoms that occupy the volume where the two lasers beams overlap. With the optimal positioning of the laser beams this volume corresponds to a narrow (3 mm diameter) cylinder located centrally on axis with the atom beam, close to the exit of the hot cavity. The technique has been successfully used in the past for nuclear structure investigations via hyperfine structure analysis of $^{97\text{-}99}$Tc,[51] $^{143\text{-}147}$Pm,[52] and $^{249\text{-}253}$Cf.[53] The PI-LIST version employed in this work is identical to the units recently adapted for ISOLDE operation, featuring the perpendicular laser access by internal metal mirror surfaces.[13]

The atomizer in operation at the ISOLDE Offline-2 mass separator laboratory[54] is a standard ISOLDE target/ion source unit, where atoms are generated by evaporating a sample within the Ohmic-heated target container or an additional sample reservoir capillary and effuse through a transfer line, after which they enter an independently heated hot-cavity capillary (atomizer) of 34 mm length and 3 mm inner diameter. In the case of the measurements presented here, the target container and transfer line were omitted and the sample from the reservoir fed directly from the back of the atomizer. It is typically heated to about 2000 °C to prevent losses by wall sticking of the atoms. The Doppler broadening full-width-at-half-maximum (FWHM) of atomic transitions in this environment is calculated as $\Delta\nu = \nu_0\sqrt{8k_B T \ln 2/mc^2}$, where k_B is the Boltzmann's constant, c the speed of light and m the atomic mass, leading to approximately 1.9 GHz for the 434 nm transition of interest in ^{152}Sm.

The PI-LIST device is located directly at the output of the atomizer, separating the laser interaction region from it by a cylindrical electrode with an inner orifice of 11 mm diameter

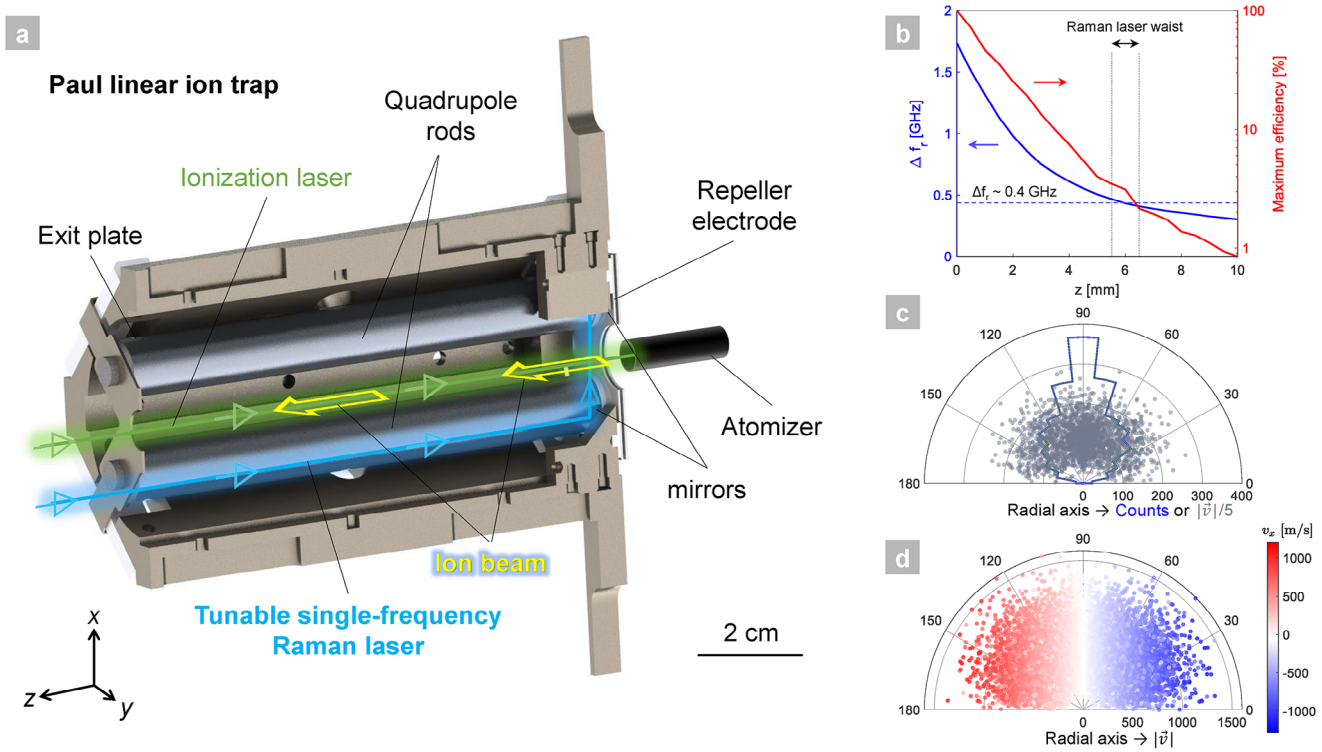

Figure 4. a) Cut-view of the Perpendicularly Illuminated Laser Ion Source and Trap (PI-LIST) system and its most relevant parts. b) Estimated PI-LIST resolution and maximum ionization efficiency as a function of distance z from the atomizer exit. c) Polar plot of the velocity distribution of atoms contained in the xz plane at $z = 0$ mm, the scale here is 1:5. The blue line is the calculated histogram per solid angle in the same plane, which corresponds to the 2D radiation pattern of the atomizer. d) Polar plot of the velocity distribution of all atoms produced in the hot cavity as a function of the angle with respect to the x-axis. The color is proportional to their v_x component, the main contributor to the Doppler broadening.

("repeller"). The cylindrical PI-LIST housing is 90 mm long and 38 mm in diameter, and in combination with an exit plate of 7 mm diameter orifice shields the interaction region in a radiofrequency quadrupole (RFQ) structure from external fields. This RFQ guides ensures radial confinement of created ions in a so-called Paul linear trap configuration, by driving them with an up to 500 V peak-to-peak RF signal at around 1 MHz. The potential at the repeller electrode is set to a positive voltage (between 7 and 50 V) such that the ions produced inside the atomizer are repelled, while the ions created inside the LIST structure are guided towards extraction. This provides high selectivity as parasitic, non-laser related ionization mechanisms in the hot atomizer are suppressed, although at the cost of overall ion extraction efficiency. After extraction as an ion beam by a 30 kV potential difference of target/ion source unit and ion beam line, the ions are separated by mass-to-charge ratio in a dipole sector field magnet and subsequently detected in a Faraday cup.

With a view on estimating an upper limit for the spectral resolution of the PI-LIST setup in our experimental conditions, we have used an effusion model capable of calculating the ion momentum distribution at the output of the atomizer and simulate the interaction with our laser beams. Previous estimations were based on model descriptions for molecule emersion from both simple orifices and elongated tubular connections between two reservoir volumes based on kinetic gas theory. In the low pressure regime, where the mean free path of the ions is considerably larger than the geometric dimensions of the ion source, the process is governed by individual trajectory evolution of the particles within the outer boundaries and not by particle collisions.

Here we present end-to-end particle tracing multiphysics simulations of a full ISOLDE-type target/ion source unit including thermal and effusion effects to estimate the spectral resolution of the PI-LIST system statistically. First, the COMSOL Heat Transfer Module was used for the thermal calculations, taking into account the effects imparted by temperature distributions in the different elements of the system. Second, the Particle Tracing Module was used to simulate the effusion process for the neutral species to be transported from the target where the atoms are produced all the way to the ion source, calculating and tracing the trajectories of both charged and neutral particles that can interact with the boundaries and their motion can be affected by various forces. Our simulations are based on previous models by Liu and colleagues described in ref. [55], and more details about it can be found in the Supporting Information.

Figure 4b shows the PI-LIST resolution Δf_r and the relative geometric ionization efficiency (i.e. atom density at a given time) ϵ are plotted as a function of z, yielding comparable results to the experimentally measured ones.[56] Due to the waist size of the interacting laser beams, the average spectral resolution $\overline{\Delta f_r}$ is the result of the combined effects of the slice resolution $\Delta f_r(z)$, the efficiency $\epsilon(z)$ and the beam profile. For our particular experimental scenario, the laser beam was intersecting the ion beam at $z = 6$ mm with a Gaussian beam diameter of around 1 mm ($1/e^2$), yielding an estimated resolution of $\overline{\Delta f_r} \approx 0.4$ GHz. We note that

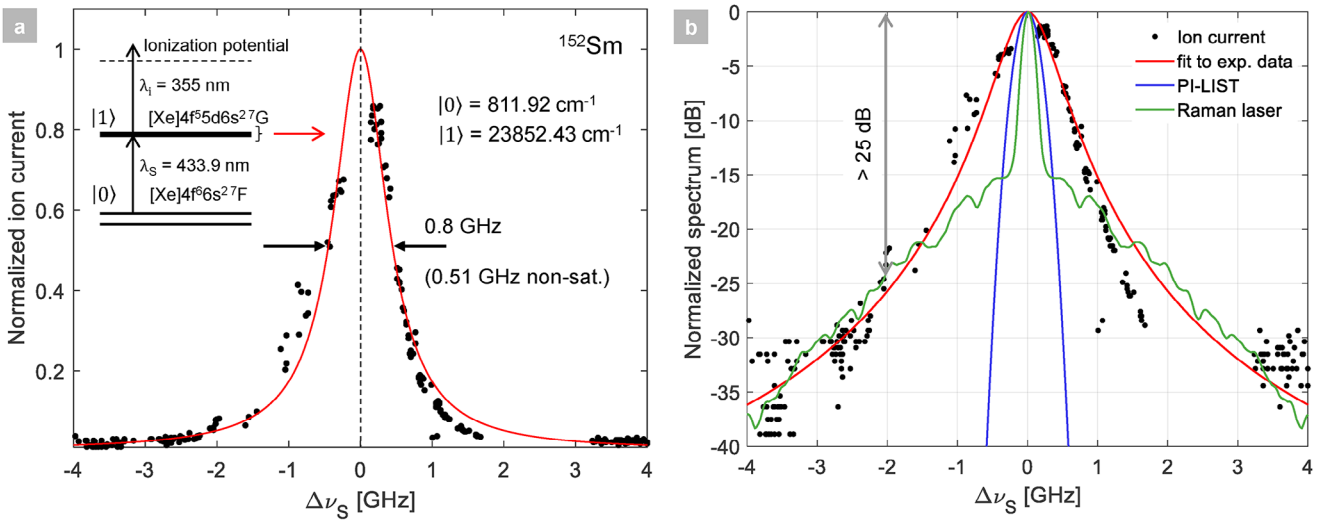

Figure 5. a) Results of measured ion current for a range of Stokes center frequency detuning. (inset) Ionization scheme, with details about the energy of the states, the energies of the wavelengths and the electronic configuration. b) Comparison of the measured absorption spectrum with the modeled Raman laser and the simulated Gaussian-like PI-LIST spectra. The results show a side-mode supression at 2 GHz >25 dB.

this value is slightly higher than the experimental one reported in previous works[13] for a comparable Doppler broadening environment, which was of the order of 200 – 300 MHz.

The directivity of the ion source was estimated by calculating the histogram of particle angles (equivalent to a radiation pattern) in the *xz* plane, and it is assumed to be axisymmetric about the *z* axis. Figure 4c shows in blue such a radial histogram, which is notably different (less directional) to the one shown in [56] for simple tubular geometries. The polar plot is accompanied by the scattered distribution showing the velocity vector magnitudes of the particles in the *xz* plane. Here, the velocity distribution spreads from 250 to 1000 m s^{-1} for angles between 30° and 150°, with a larger contribution in a narrower cone between 70° and 110°, and an average particle velocity of 600 m s^{-1}.

Figure 4d shows a scatter polar plot of all the particles escaping the hot cavity, where we plot against the angle between the particle velocity vector $\vec{v}_i$ and the *x* axis. The plot also shows the magnitude of $|\vec{v}_i|$, and the color represents its scalar component on the *x* axis (v_{xi}) contributing to the Doppler effect. It is clear from this analysis that both the particle density per solid angle, and its velocity distribution needs to be taken into account simultaneously for the overall estimation of the resolution of the PI-LIST device.

4. Results and Conclusion

The primary goal of the in-source spectroscopy setup described here was to prove the suitability of an integrated single-frequency Raman laser for high resolution spectroscopy applications. For our experiment we took measurements of the temperature of the diamond, the Stokes field frequency, linewidth and the resulting ion current simultaneously.

The selected two-step ionization scheme starts by targeting a thermally populated, low-lying fine structure component of the atomic ground state of ^{152}Sm, with structure [Xe] 4f^6 6s^2 ^{7}F and total angular momentum J = 2. It is situated at an energy corresponding to 811.92 cm^{-1} above the actual ground state. The single-frequency Raman laser at 433.9 nm excites the electrons to the state [Xe]4f^{5}5d6s^2 ^{7}G, J = 3, at 23,852.43 cm^{-1}. State energies and configurations were taken from ref. [57]. The second step at 355 nm is non-resonant and provides the photon energy required for the excited electrons to escape the atoms, and thus permitting the PI-LIST to fulfil its goal and provide us with the wanted ions. The mass-separated ion current readout as a function of laser wavelength results in a lineshape proportional to the spectral absorption line of the transition of interest.

The ^{152}Sm transition of interest here is from the state 4f^{6}6s^2 ^{7}F$_2$ → 4f^{5}5d6s^2 ^{7}G$_3$, a frequency step from 811.92 to 23,852.43 cm^{-1}, requiring a Raman laser centered around ν_s = 23,040.51 cm^{-1} (433.9 nm). The required wavelength of the Raman laser was achieved by first tuning the wavelength of the pump Ti:Sapphire laser to 409.3 nm, while the fine sub-GHz-class tuning during the experiment was done exclusively using the temperature of the Raman resonator.

The result of such a scan can be seen in **Figure 5**a, where the FWHM of the transition was measured to be around 0.8 GHz. Since the target transition linewidth was negligible compared to the instrumental width of the PI-LIST and the linewidth of the Raman laser, this setup can measure the resolution of the instrumentation accurately.

The laser power was of sufficient intensity to add additional broadening of the optical resonance linewidth under study, which occurred with a few mW coming from the Raman laser. The power was reduced to values below the level of saturation at the cost of overall signal to noise ratio (to approximately a 40 dB range). The saturation effect (also referred to as power broadening) on the measured transition linewidth can be fitted with a saturated Lorentzian function as follows: $\alpha(\Delta\nu_s) \propto L(\Delta\nu_s) \times (1/(1 + SL(\Delta\nu_s)))$, where S is a saturation parameter that depends on the overall laser intensity, $\Delta\nu_s$ the laser detuning and $L(\Delta\nu_s)$ is a Lorentzian function with width as the unsaturated linewidth of the transition.[29] The result of this fitting retrieves an

unsaturated width of 0.51 GHz at FWHM. Compare this to the convolution of the laser linewidth ($\Delta\nu_s \simeq 300$ MHz, Gaussian lineshape) and the PI-LIST resolution ($\Delta f_r \simeq 0.4$ GHz, Gaussian lineshape) which is around $\Delta\nu_{res} = \sqrt{\Delta f_r^2 + \Delta\nu_s^2} \simeq 0.5$ GHz. From this result we believe that the Monte Carlo effusion model used to calculate the PI-LIST spectral resolution is indeed in good agreement with the experiments. The earlier mentioned discrepancy to other experimental results obtained with the PI-LIST, possibly also due to unidentified additional broadening effects, is subject to upcoming further investigations and refinements of the model. This will include ion survival considerations in the PI-LIST electric fields, accompanied by systematic experimental measurements of the dependence of resolution and efficiency from distance to the atomizer.

There are other effects that could be included, such as the contribution to the current caused by non-resonant ionization and linear with laser power, if the photon energy is sufficiently high. From this consideration it is evident that the absorption cross-section of a transition may not directly be translated into a corresponding ionization rate but also has a non-linear dependency on the incident laser power.

A comparison between the retrieved spectroscopy measurement and the spectral content of the laser reveals that the computational model may slightly overestimate the spectral noise of the Raman laser by a few dB, since the experimental results are a convolution of the laser spectrum, the PI-LIST spectral response and the saturated transition lineshape. In this case, it is safe to assume that the un-coated diamond Raman resonator exhibits a ratio of at least 25 dB from peak to side-mode at 2 GHz, in reasonable agreement with the theory.

To conclude, the results show that the laser technology developed here alongside with the PI-LIST device, can effectively perform high-selectivity in-source spectroscopy, with a demonstrated combined resolution of at least 0.51 GHz. This demonstration paves the way to integrated high resolution ionization spectroscopy of nuclear species below hot cavity Doppler broadening limitations, using simple integrated Raman sources. A plethora of nuclei, with hyperfine splits in the sub-GHz range are ready to be used with the present setup, holding the promise to unlock further information about the nuclear structure of elements and their application in nuclear physics and revolutionary quantum technologies.

Supporting Information

Supporting Information is available from the Wiley Online Library or from the author.

Acknowledgements

The authors would like to acknowledge the CERN Knowledge Transfer Fund project "Singular Light" for allocating the funds and time to develop the integrated Raman laser and Prof. Richard Mildren and Prof. David Spence from Macquarie University for fruitful discussions regarding the Raman laser model. The authors would also like to thank Yuan Liu and Michael S. Smith from Oak Ridge National Lab for making available COMSOL simulation files related to the generation of intense exotic radiation beams, which were incorporated in the particle tracing and PI-LIST resolution simulations.

Conflict of Interest

The authors declare no conflict of interest.

Data Availability Statement

The data that support the findings of this study are available from the corresponding author upon reasonable request.

Keywords

high-resolution spectroscopy, integrated lasers, quantum technologies, raman effect

Received: June 19, 2023
Revised: October 10, 2023
Published online: November 23, 2023

[1] M. Huang, D. K. Serkland, J. Camparo, *Appl. Phys. Lett.* **2022**, *121*, 114002.
[2] S. Gundavarapu, G. M. Brodnik, M. Puckett, T. Huffman, D. Bose, R. Behunin, J. Wu, T. Qiu, C. Pinho, N. Chauhan, J. Nohava, P. T. Rakich, K. D. Nelson, M. Salit, D. J. Blumenthal, *Nat. Photonics* **2019**, *13*, 60.
[3] H. Xu, C. Li, G. Wang, H. Wang, H. Tang, A. R. Barr, P. Cappellaro, J. Li, *Phys. Rev. X* **2023**, *13*, 011017.
[4] C. D. Bruzewicz, J. Chiaverini, R. McConnell, J. M. Sage, *Appl. Phys. Rev.* **2019**, *6*, 021314.
[5] B. A. Marsh, T. Day Goodacre, S. Sels, Y. Tsunoda, B. Andel, A. N. Andreyev, N. A. Althubiti, D. Atanasov, A. E. Barzakh, J. Billowes, K. Blaum, T. E. Cocolios, J. G. Cubiss, J. Dobaczewski, G. J. Farooq-Smith, D. V. Fedorov, V. N. Fedosseev, K. T. Flanagan, L. P. Gaffney, L. Ghys, M. Huyse, S. Kreim, D. Lunney, K. M. Lynch, V. Manea, Y. Martinez Palenzuela, P. L. Molkanov, T. Otsuka, A. Pastore, M. Rosenbusch, et al., *Nat. Phys.* **2018**, *14*, 1163.
[6] X. Yang, S. Wang, S. Wilkins, R. G. Ruiz, *Prog. Part. Nucl. Phys.* **2023**, *129*, 104005.
[7] B. B. Blinov, D. Leibfried, C. Monroe, D. J. Wineland, *Quantum Inf. Process.* **2004**, *3*, 45.
[8] Y. Kim, H.-J. Joo, M. Chen, B. Son, D. Burt, X. Shi, L. Zhang, Z. Ikonic, C. S. Tan, D. Nam, *Adv. Sci.* **2023**, *10*, 2207611.
[9] R. J. Niffenegger, J. Stuart, C. Sorace-Agaskar, D. Kharas, S. Bramhavar, C. D. Bruzewicz, W. Loh, R. T. Maxson, R. McConnell, D. Reens, G. N. West, J. M. Sage, J. Chiaverini, *Nature* **2020**, *586*, 538.
[10] M. A. Tran, C. Zhang, T. J. Morin, L. Chang, S. Barik, Z. Yuan, W. Lee, G. Kim, A. Malik, Z. Zhang, J. Guo, H. Wang, B. Shen, L. Wu, K. Vahala, J. E. Bowers, H. Park, T. Komljenovic, *Nature* **2022**, *610*, 54.
[11] M. Corato-Zanarella, A. Gil-Molina, X. Ji, M. C. Shin, A. Mohanty, M. Lipson, *Nat. Photonics* **2023**, *17*, 157.
[12] V. Fedosseev, K. Chrysalidis, T. D. Goodacre, B. Marsh, S. Rothe, C. Seiffert, K. Wendt, *J. Phys. G* **2017**, *44*, 084006.
[13] R. Heinke, M. Au, C. Bernerd, K. Chrysalidis, T. E. Cocolios, V. N. Fedosseev, I. Hendriks, A. A. Jaradat, M. Kaja, T. Kieck, T. Kron, R. Mancheva, B. A. Marsh, S. Marzari, S. Raeder, S. Rothe, D. Studer, F. Weber, K. Wendt, *Nucl. Instrum. Methods Phys. Res. Sect. B* **2023**, *541*, 8.
[14] K. K. Mehta, C. Zhang, M. Malinowski, T.-L. Nguyen, M. Stadler, J. P. Home, *Nature* **2020**, *586*, 533.
[15] Z. Bai, Z. Zhao, M. Tian, D. Jin, Y. Pang, S. Li, X. Yan, Y. Wang, Z. Lu, *Microw. Opt. Technol. Lett.* **2022**, *64*, 2244.

[16] N. Chauhan, A. Isichenko, K. Liu, J. Wang, Q. Zhao, R. O. Behunin, P. T. Rakich, A. M. Jayich, C. Fertig, C. W. Hoyt, D. J. Blumenthal, *Nat. Commun.* **2021**, *12*, 4685.
[17] V. Sonnenschein, I. D. Moore, S. Raeder, M. Reponen, H. Tomita, K. Wendt, *Laser Phys.* **2017**, *27*, 085701.
[18] V. Sonnenschein, H. Tomita, *Appl. Sci.* **2022**, *12*, 9.
[19] E. Granados, D. J. Spence, R. P. Mildren, *Opt. Express* **2011**, *19*, 10857.
[20] G. Demetriou, A. J. Kemp, V. Savitski, *Opt. Express* **2019**, *27*, 10296.
[21] O. Lux, S. Sarang, R. J. Williams, A. McKay, R. P. Mildren, *Opt. Express* **2016**, *24*, 27812.
[22] O. Kitzler, J. Lin, H. M. Pask, R. P. Mildren, S. C. Webster, N. Hempler, G. P. A. Malcolm, D. J. Spence, *Opt. Lett.* **2017**, *42*, 1229.
[23] X. Yang, Z. Bai, D. Chen, W. Chen, Y. Feng, R. P. Mildren, *Opt. Express* **2021**, *29*, 29449.
[24] X. Yang, O. Kitzler, D. J. Spence, R. J. Williams, Z. Bai, S. Sarang, L. Zhang, Y. Feng, R. P. Mildren, *Opt. Lett.* **2019**, *44*, 839.
[25] S. Sarang, O. Kitzler, O. Lux, Z. Bai, R. J. Williams, D. J. Spence, R. P. Mildren, *OSA Continuum* **2019**, *2*, 1028.
[26] P. Latawiec, V. Venkataraman, M. J. Burek, B. J. M. Hausmann, I. Bulu, M. Lončar, *Optica* **2015**, *2*, 924.
[27] P. Latawiec, V. Venkataraman, A. Shams-Ansari, M. Markham, M. Lončar, *Opt. Lett.* **2018**, *43*, 318.
[28] K. Chrysalidis, V. N. Fedosseev, B. A. Marsh, R. P. Mildren, D. J. Spence, K. D. A. Wendt, S. G. Wilkins, E. Granados, *Opt. Lett.* **2019**, *44*, 3924.
[29] D. T. Echarri, K. Chrysalidis, V. N. Fedosseev, R. Heinke, B. A. Marsh, B. B. Reich, E. Granados, *Front Phys.* **2022**, *10*, 937976.
[30] R. Casula, J.-P. Penttinen, M. Guina, A. J. Kemp, J. E. Hastie, *Optica* **2018**, *5*, 1406.
[31] D. T. Echarri, K. Chrysalidis, V. N. Fedosseev, B. A. Marsh, R. P. Mildren, S. M. Olaizola, D. J. Spence, S. G. Wilkins, E. Granados, *Opt. Express* **2020**, *28*, 8589.
[32] E. Granados, C. Granados, R. Ahmed, K. Chrysalidis, V. N. Fedosseev, B. A. Marsh, S. G. Wilkins, R. P. Mildren, D. J. Spence, *Optica* **2022**, *9*, 317.
[33] E. Granados, G. Stoikos, *Opt. Lett.* **2022**, *47*, 3976.
[34] Z. Yu, X. Sun, *ACS Photonics* **2021**, *8*, 798.
[35] E. Granados, G. Stoikos, D. T. Echarri, K. Chrysalidis, V. N. Fedosseev, C. Granados, V. Leask, B. A. Marsh, R. P. Mildren, *Appl. Phys. Lett.* **2022**, *120*, 151101.
[36] G. Stoikos, E. Granados, *Phys. Rev. A* **2022**, *106*, 023504.
[37] D. J. Spence, *Prog. Quantum Electron.* **2017**, *51*, 1.
[38] G. P. Dzhotyan, Y. E. D'yakov, I. G. Zubarev, A. B. Mironov, S. I. Mikhaĭlov, *Soviet J. Quantum Electron.* **1977**, *7*, 783.
[39] V. G. Sidorovich, *Soviet J. Quantum Electron.* **1978**, *8*, 784.
[40] W. Trutna, Y. Park, R. Byer, *IEEE J. Quantum Electron.* **1979**, *15*, 648.
[41] C. Warner, B. Bobbs, *J. Opt. Soc. Am. B* **1986**, *3*, 1345.
[42] L. A. Westling, M. G. Raymer, *Phys. Rev. A* **1987**, *36*, 4835.
[43] Y. Xiong, S. Murphy, J. L. Carlsten, K. Repasky, *J. Opt. Soc. Am. B* **2007**, *24*, 2055.
[44] K. Jia, X. Wang, D. Kwon, J. Wang, E. Tsao, H. Liu, X. Ni, J. Guo, M. Yang, X. Jiang, J. Kim, S.-n. Zhu, Z. Xie, S.-W. Huang, *Phys. Rev. Lett.* **2020**, *125*, 143902.
[45] G. Turri, S. Webster, Y. Chen, B. Wickham, A. Bennett, M. Bass, *Opt. Mater. Express* **2017**, *7*, 855.
[46] P. Jacobson, S. Stoupin, *Diamond Relat. Mater.* **2019**, *97*, 107469.
[47] R. Heinke, T. Kron, S. Raeder, T. Reich, P. Schönberg, M. Trümper, C. Weichhold, K. Wendt, *Hyperfine Interact.* **2016**, *238*, 6.
[48] D. Fink, S. Richter, K. Blaum, R. Catherall, B. Crepieux, V. Fedosseev, A. Gottberg, T. Kron, B. Marsh, C. Mattolat, S. Raeder, R. Rossel, S. Rothe, F. Schwellnus, M. Seliverstov, M. Sjödin, T. Stora, P. Suominen, K. Wendt, *Nucl. Instrum. Methods Phys. Res. Sect. B* **2015**, *344*, 83.
[49] D. Fink, S. Richter, B. Bastin, K. Blaum, R. Catherall, T. Cocolios, D. Fedorov, V. Fedosseev, K. Flanagan, L. Ghys, A. Gottberg, N. Imai, T. Kron, N. Lecesne, K. Lynch, B. Marsh, T. Mendonca, D. Pauwels, E. Rapisarda, J. Ramos, R. Rossel, S. Rothe, M. Seliverstov, M. Sjödin, T. Stora, C. Van Beveren, K. Wendt, *Nucl. Instrum. Methods Phys. Res. Sect. B* **2013**, *317*, 417.
[50] R. Catherall, W. Andreazza, M. Breitenfeldt, A. Dorsival, G. J. Focker, T. P. Gharsa, G. T. J, J.-L. Grenard, F. Locci, P. Martins, S. Marzari, J. Schipper, A. Shornikov, T. Stora, *J. Phys. G: Nucl. Part. Phys.* **2017**, *44*, 094002.
[51] D. A. Fink, T. E. Cocolios, A. N. Andreyev, S. Antalic, A. E. Barzakh, B. Bastin, D. V. Fedorov, V. N. Fedosseev, K. T. Flanagan, L. Ghys, A. Gottberg, M. Huyse, N. Imai, T. Kron, N. Lecesne, K. M. Lynch, B. A. Marsh, D. Pauwels, E. Rapisarda, S. D. Richter, R. E. Rossel, S. Rothe, M. D. Seliverstov, A. M. Sjödin, C. Van Beveren, P. Van Duppen, K. D. A. Wendt, *Phys. Rev. X* **2015**, *5*, 011018.
[52] D. Studer, J. Ulrich, S. Braccini, T. S. Carzaniga, R. Dressler, K. Eberhardt, R. Heinke, U. Köster, S. Raeder, K. Wendt, *Eur. Phys. J. A* **2020**, *56*, 69.
[53] F. Weber, T. E. Albrecht-Schönzart, S. O. Allehabi, S. Berndt, M. Block, H. Dorrer, C. E. Düllmann, V. A. Dzuba, J. G. Ezold, V. V. Flambaum, V. Gadelshin, S. Goriely, A. Harvey, R. Heinke, S. Hilaire, M. Kaja, T. Kieck, N. Kneip, U. Köster, J. Lantis, C. Mokry, D. Münzberg, S. Nothhelfer, S. Oberstedt, S. Péru, S. Raeder, J. Runke, V. Sonnenschein, M. Stemmler, D. Studer, et al., *Phys. Rev. C* **2023**, *107*, 034313.
[54] S. Warren, T. Giles, C. Pequeno, A. Ringvall-Moberg, *Nucl. Instrum. Methods Phys. Res. Sect. B* **2020**, *463*, 115.
[55] Y. Liu, M. S. Smith, Computational Studies of Solid Stoppers for Generating Intense Exotic Radioactive Ion Beams at FRIB, https://www.osti.gov/biblio/1484136, (accessed: June- 2023).
[56] R. Heinke, V. Fedosseev, T. Kieck, T. Kron, B. Marsh, S. Raeder, S. Richter, S. Rothe, K. Wendt, *Nucl. Instrum. Methods Phys. Res., Sect. B* **2020**, *463*, 449.
[57] A. Kramida, Yu. Ralchenko, J. Reader, and NIST ASD Team, NIST Atomic Spectra Database, Gaithersburg, MD, https://physics.nist.gov/asd, June **2022**.